ACS APPLIED ENERGY MATERIALS

www.acsaem.org

Article

Surface-Modified Compressed Expanded Graphite for Increased Salt Hydrate Phase Change Material Thermal Conductivity and Stability

Erin Blackley, Trinny Lai, Adewale Odukomaiya,* Paulo Cesar Tabares-Velasco, Lance M. Wheeler, and Jason Woods

Cite This: *ACS Appl. Energy Mater.* 2023, 6, 8775−8786

Read Online

ACCESS | Metrics & More | Article Recommendations

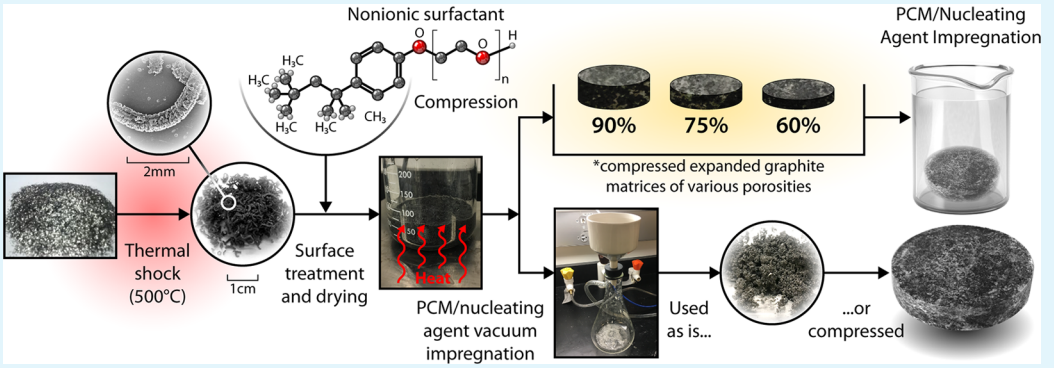

ABSTRACT: Thermal energy storage (TES) will play an essential role in the push toward efficient, electrified buildings, and phase change materials (PCMs) offer a high potential to fill that need. While organic PCMs have been studied extensively for TES, the literature on inorganic PCMs such as salt hydrates is scarce despite their advantages. Calcium chloride hexahydrate ($CaCl_2 \cdot 6H_2O$, CCH) has a phase transition temperature of interest for buildings' heating/cooling applications but like other salt hydrates, suffers from supercooling, phase separation, and low thermal conductivity. Researchers have proposed strontium chloride hexahydrate ($SrCl_2 \cdot 6H_2O$, SCH) as an effective lattice-matched nucleating agent for CCH; additionally, porous compressed expanded graphite (EG) offers thermal conductivity enhancement along with form stability. This paper presents the fabrication of a PCM composite consisting of CCH, nucleating agent SCH, and surface-modified EG using a nonionic surfactant, which addresses the concerns related to salt hydrates while providing excellent cycling stability on a larger scale. The contributions of this study include (1) high thermal conductivity (4 ± 0.2 W/m·K), (2) a significant reduction in supercooling (less than 1 °C), (3) high composite latent heat (up to 183 J/g), and (4) eliminated phase separation demonstrated via improved cycling stability with no reduction in latent heat for up to 200 cycles.

KEYWORDS: *thermal energy storage, salt hydrate phase change material, expanded graphite, thermal conductivity enhancement, supercooling mitigation, phase separation prevention*

1. INTRODUCTION

The buildings sector is responsible for about one-third of the total worldwide energy consumption and contributes about 28% of CO_2 emissions,[1] with expansion and growth expected in the coming years.[2] Currently, heating, ventilation, and air conditioning (HVAC) is the single most consuming electric end use worldwide, accounting for 12% of all energy consumed[3] and more than 50% of energy consumed in buildings.[4] In many places, such as the United States, where 90% of households own some form of air-conditioning system, HVAC can account for up to 70% of peak residential electric demand in the summer.[5] Energy storage is a prominent solution for managing electric loads: among a number of storage technologies, thermal energy storage (TES) can improve thermal management by minimizing the mismatch between supply and demand in heating and cooling.[6] Phase change materials (PCMs) have been widely studied for applications in TES for buildings because of their inherently high energy storage density resulting from a high latent heat of fusion. By utilizing latent heat, a lower volume of PCM can store 5−14 times more energy than materials such as concrete,

Received: May 15, 2023
Accepted: August 18, 2023
Published: August 28, 2023

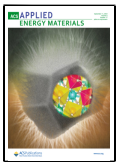

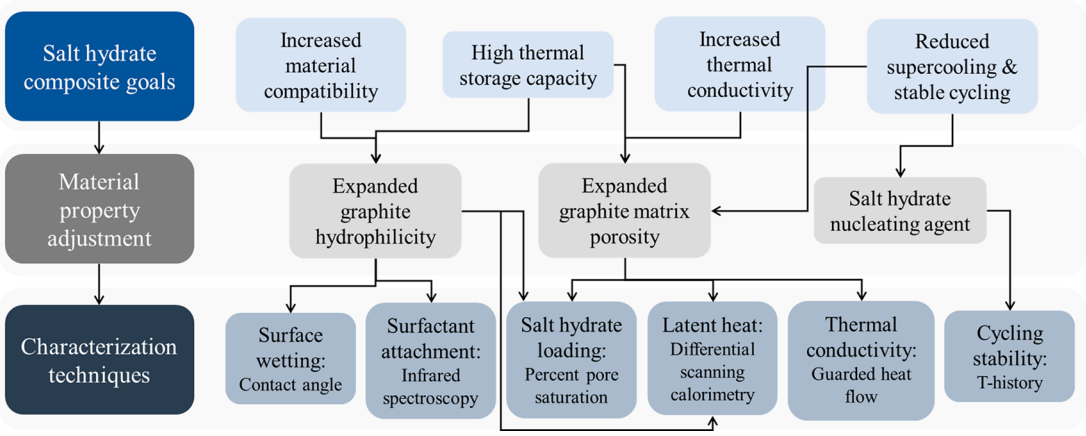

Figure 1. Flowchart displaying the overall process used to address salt hydrate challenges and the techniques used to characterize the material properties.

bricks, or wood, which can only store thermal energy in the form of sensible heat.[7] Ultimately, this technology allows for improved regulation of thermal comfort while also reducing or shifting HVAC loads. Some experimental studies demonstrating the benefits of PCMs in HVAC systems include modular PCM storage as part of a heat pump air system,[8] PCM plates integrated into the condenser of an air-conditioning unit,[9] and PCM-integrated air-conditioning ducts.[10]

PCMs are generally split into three material categories: organic, inorganic, and eutectic.[3,10] Organic PCMs such as paraffins are attractive because they offer a wide range of available transition temperatures, a high heat storage capacity, little-to-no supercooling, chemical stability, and good compatibility with other materials. However, they suffer from low thermal conductivity, large volume change during the phase change, and flammability.[11] Inorganic PCMs such as salt hydrates, however, have a higher heat storage capacity, higher thermal conductivity, sharp melting point, lower phase change volume effect, nonflammability, and lower cost.[12−14] However, salt hydrates are prone to supercooling, phase separation, and corrosion, which has led to a lag in technology development and deterred widespread adoption despite their advantages.[15]

Supercooling, a major challenge inherent to inorganic PCMs, can be mitigated by promoting nucleation via increased surface area and decreased surface tension (i.e., wetting) of the PCM melt against solid surfaces.[16−18] Previous studies have investigated the addition of high specific surface area matrixes[19−22] and lattice-matched nucleating agents[23−25] to mitigate supercooling. Phase separation is an additional challenge associated with salt hydrate PCMs, where incongruent or semicongruent melting leads to separate solid and liquid phases consisting of anhydrous salt hydrate, salt hydrate, and salt solution,[15] ultimately leading to decreased enthalpy. If cooling occurs quickly (uncommon in practical PCM applications) or solid and liquid phases are kept in micro/nanoproximity to each other, phase separation can be mitigated.

Salt hydrates, like most other pure PCMs, also suffer from low thermal conductivity (~0.3−0.9 W/mK),[26,27] preventing adequate charge/discharge rates in practical applications. The addition of a material with high thermal conductivity, such as graphite, graphene, carbon nanotubes, metal oxide nanoparticles, metal foams, expanded graphite (EG), and clay minerals, has been studied for thermal conductivity enhancement of PCMs,[28,29] although most of these studies were conducted on organic PCMs. Shape-stabilized composites, characterized by a PCM incorporated into a highly porous matrix such as EG or nanoscale networks such as carbon nanotubes, show reliable, improved performance due to reduced leakage and the potential for thermal conductivity enhancement.[6,30] EG in particular also features a high specific surface area, a characteristic that can help reduce supercooling and phase separation[31] as well as PCM leakage when modified with TX-100 surfactant.[32−34] EG[35,36] matrixes are well-known for enhancing the thermal conductivity of organic paraffin PCMs[37−45] and organic eutectic PCMs.[46] However, there are few efforts that utilize EG in inorganic salt hydrate PCM composites, largely because of challenges in impregnating nonpolar, hydrophobic EG with polar, hydrophilic salt hydrates.

Calcium chloride hexahydrate ($CaCl_2{\cdot}6H_2O$, CCH) is a salt hydrate PCM that is particularly attractive for building HVAC applications because of its melting temperature (~28 °C). Researchers have successfully impregnated CCH into EG matrixes by introducing hydrophilicity on the surface of EG using surfactants such as OP-10[47] and sodium dodecyl benzenesulfonate[48] as well as oxide nanoparticles such as $NiCO_2O_4$.[49] Strontium chloride hexahydrate ($SrCl_2{\cdot}6H_2O$, SCH) has demonstrated successful nucleation enhancement for CCH,[48,50,51] showing a decrease in supercooling in addition to the nucleation sites provided by EG.

While a few previous studies have shown promising integration of EG with salt hydrates for applications in TES,[47,49,51] there is a demonstrated need to produce a composite that addresses all of the challenges inherent to salt hydrates while also maintaining long-term thermal performance on sample sizes larger than a few milligrams. While the studies cited previously do offer solutions to address salt hydrate challenges such as thermal conductivity and supercooling, many do not do so synergistically. For the barrier of entry for salt hydrates in buildings-related TES applications to be lowered enough for market adoption, such challenges must be addressed in one composite material. Namely, most studies on the cycling stability of salt hydrates rely on differential scanning calorimetry (DSC) data to demonstrate reduced supercooling and maintenance of enthalpy throughout cycling. However, DSC cannot be considered representative of practical applications because of the small (<10 mg) sample

https://doi.org/10.1021/acsaem.3c01223
ACS Appl. Energy Mater. 2023, 6, 8775−8786

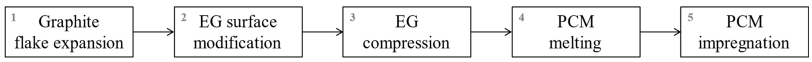

Figure 2. Flowchart describing the general procedure for producing the EG PCM composite.

sizes used.[52] Niu et al.[51] describes larger-scale testing but only observed the behavior of the composite material over one thermal charge/discharge cycle.

While previous studies have investigated composites consisting of surface-modified EG and CCH, no single study to date has shown the successful long-term performance of a CCH composite on a scale larger than DSC. This study presents the synthesis of a novel form-stable composite consisting of CCH with lattice-matched nucleating agent SCH impregnated into surface-modified EG using octylphenol ethoxylate surfactant (TX-100).[53] The results of this study contribute to the field of PCMs by demonstrating (1) high PCM loading of the EG matrix, (2) significant thermal conductivity enhancement, (3) high latent heat storage capacity, (4) near elimination of supercooling, and (5) stable long-term cycling behavior on a larger scale. Thus, this study addresses all salt hydrate material challenges and holistically meets the deficits in salt hydrate/EG composite research, ultimately expanding opportunities for this technology in the TES market.

2. METHODS

Figure 1 shows the overall methodology featured in this work, starting from the materials-based goals, the methods used to achieve such goals, and the characterization techniques used to validate the effectiveness of the proposed methods in achieving the goals.

2.1. Materials. Expandable graphite flakes (product no. EG-150-230) were purchased from ACS Materials. $CaCl_2{\cdot}6H_2O$ (CCH; ≥99% purity), $SrCl_2{\cdot}6H_2O$ (SCH; 99% purity), and laboratory-grade octylphenol ethoxylate surfactant (TX-100) were purchased from Sigma-Aldrich.

2.2. Preparation of the PCM Composite. The general procedure for preparing impregnated, surface-modified EG is shown in Figure 2 and follows the methods described below, where each step corresponds to a block in the flowchart.

2.2.1. Graphite Flake Expansion. After preheating an oven to 500 °C, we placed small amounts of expandable graphite flakes in a large beaker, covered the beaker with aluminum foil to prevent loss of material during expansion, and placed it in the preheated oven for 5 min. The hot environment induced a thermal shock, where a nearly instantaneous evaporation of the intercalating agent in the flakes (sulfuric acid, nitric acid, and the oxidizing agent) caused a violent expansion. The thermal shock produced "worms" of about 99% porosity. EG is responsible for providing shape stabilization of the composite as well as thermal conductivity enhancement for CCH.

2.2.2. EG Surface Modification. Equation 1 provides the calculation for TX-100/EG mass ratio $x_{S:EG}$, which we used to determine the concentration of surfactant used for surface modification, where m_S is the surfactant mass and m_{EG} is the EG mass. For experimentation, we chose ratios between 0.01 and 0.05.

$$x_{S:EG} = \frac{m_S}{m_{EG}} \tag{1}$$

On the basis of the desired surfactant concentration, we added TX-100 to about 10 mL of deionized water and sonicated the solution until well dispersed (about 10 min). After adding the corresponding amount of EG to the solution and allowing it to soak for at least 1 h, we removed the wet EG and dried it in a furnace at 100−110 °C overnight to remove water from the pores. The soaking and drying procedure resulted in surface-modified, hydrophilic EG, which promotes the impregnation of hydrophobic CCH into the pores of EG and maximizes the energy density of the composite.

2.2.3. EG Compression. To produce compressed EG disks, we placed the EG worms in a pellet die and used a hydraulic press with a range of compressive forces. The magnitude of the applied force corresponded to an approximate EG disk porosity ranging from 60% to 90%. Equation 2 gives the EG disk porosity, where ρ_{CENG} is the bulk density of the compressed matrix (mass divided by volume) and ρ_G is the density of crystal graphite,[54] taken as 2.09 g/cm^3.

$$\varphi = 1 - \frac{\rho_{CENG}}{\rho_G} \tag{2}$$

Taking into consideration the slightly reduced porosity due to the presence of surfactant in surface-modified EG, eq 3 gives effective density ρ_{ED}, where m_{EG} is the mass of the untreated EG, m_{EG+S} is the total mass (EG + surfactant), and ρ_S is the density of the surfactant provided by the manufacturer. In the case of a precompression surface treatment, we calculated the disk porosity using eq 2 but replaced ρ_G with ρ_{ED}.

$$\rho_{ED} = \frac{m_{EG}}{m_{EG+S}}\rho_G + \frac{m_S}{m_{EG+S}}\rho_S \tag{3}$$

We used different pellet dies to create disks for different experiments: 3 mm diameter for DSC, 40 mm diameter for saturation experiments, and 50 mm diameter for thermal conductivity. Compression of EG was necessary in order to provide a higher degree of shape stabilization and tailor the porosity of EG for experimentation.

2.2.4. PCM Melting. For experiments investigating only CCH without a nucleating agent, we prepared molten PCM by adding solid CCH to a sealed Nalgene bottle submerged in a water bath at 70 °C. For experiments investigating the effectiveness of nucleating agent addition, we added specified concentrations of SCH to the Nalgene bottle containing CCH, this time submerged in a water bath at 150 °C. Molten PCM is necessary for the successful impregnation of CCH into the pores of EG. After impregnation, when CCH returns to room temperature, it solidifies again and can thus undergo cycling between liquid and solid states.

2.2.5. PCM Impregnation. After melting the PCM in Nalgene, we transferred the molten PCM to a small beaker on a hot plate at 70 °C for pure CCH and 150 °C for CCH with SCH. We added EG to the beaker with molten PCM and placed aluminum foil over the beaker to mitigate evaporative water loss during soaking. To ensure maximum possible pore saturation for all testing, we incrementally removed EG from the molten PCM, patted off excess PCM with a Kimwipe, and recorded the mass of the soaked EG until the mass no longer increased. Afterward, we removed excess PCM one last time, covered the soaked EG, and allowed it to rest at room temperature until PCM solidified. To validate the extent of PCM impregnation, we used eq 4 to calculate the theoretical volumetric impregnation limit V_{max} for each porosity and eq 5 to calculate the experimental percent pore saturation of the EG disk. In eq 4, h represents the height of the compressed disk and d represents the diameter of the pellet die used; in eq 5, m_f represents the mass of the final disk after soaking and ρ_{PCM} represents the density of CCH.

$$V_{max} = \varphi h\left(\frac{\pi d^2}{4}\right) \tag{4}$$

$$\varphi_{sat.} = \frac{m_f - m_{EG+S}}{\rho_{PCM} V_{max}} \tag{5}$$

To prepare impregnated, uncompressed EG worms, we followed the same soaking procedure, but rather than removing the EG incrementally, we used a stir bar to mix the worms in the molten PCM bath for about 1 h. Then, we transferred the soaked EG worms

https://doi.org/10.1021/acsaem.3c01223
ACS Appl. Energy Mater. 2023, 6, 8775−8786

Table 1. List of Properties Studied, Corresponding Input Values, Investigative Purpose, and Relevant Figures

Property	Investigated parameters	Experimental purpose	Relevant figure(s)
EG matrix porosity (%)	60 75 90	PCM infiltration/loading	6, 7, 8, 10
TX-100:EG mass fraction	0 0.02 0.03 0.04 0.05	TX-100 incorporation, PCM loading	5, 7, 8
Surface modification method	EG pre-compression EG post-compression	EG surface modification	4
SCH concentration (wt% of CCH)	0 1 2 5	Phase separation, supercooling, cycling stability	9

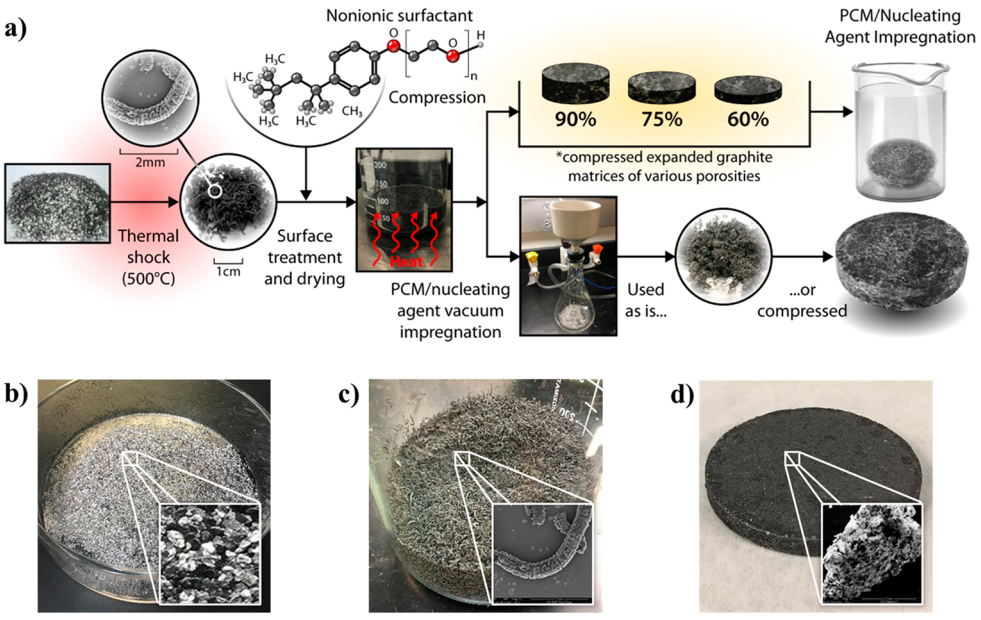

Figure 3. (a) Complete synthesis process for PCM/surface-modified EG matrixes, including thermal shock and expansion, surface treatment, compression, and impregnation. (b) Expandable graphite flakes pre-expansion with a magnified SEM image. (c) EG worm post-expansion with a magnified SEM image. (d) Compressed EG disk of ∼60% porosity with a magnified SEM image.

immediately to a ceramic filter and removed the excess PCM via vacuum filtration. We covered the filtered EG and left it to rest until the PCM solidified.

During experimentation, we used EG in uncompressed, compressed, unmodified, and modified forms. Table 1 includes the values investigated and used to determine the optimal TX-100 concentration, EG disk porosity, and surface modification method (described further in Section 3.1).

2.3. Characterization Methods. On the basis of the variables shown in Table 1, we used the following techniques to characterize the material properties of the PCM composite throughout experimentation. Most characterization occurred sequentially because the results of any given test informed the composition of a subsequent PCM composite, as well as the design of subsequent characterization. We chose to use the following methods in order to ensure that the composite met all of the goals set out in Figure 1.

2.3.1. Surface Wetting. To determine the effectiveness of different surface modification methods, we used a Krüss Drop Shape Analyzer 100 (DSA) and associated software to collect measurements and images of molten CCH on various compressed EG substrates.

2.3.2. Nanoscale Imaging. To gain visual insight into the morphology of the materials that we worked with, we used an FEI Quantum 600 scanning electron microscope (SEM) to image samples of graphite and PCM in all stages of preparation (such as those shown in Figure 3). During imaging, we used an accelerating voltage of 7 kV.

2.3.3. Functional Group Identification. For molecular validation of EG surface modification, we performed diffuse-reflectance infrared Fourier transform spectroscopy (DRIFTS) on a Bruker Alpha FTIR spectrometer inside a nitrogen-atmosphere glovebox and collected spectra by averaging 24 scans at 2 cm^{-1} resolution. Samples consisted of surface-modified EG on an aluminum-coated silicon wafer.

2.3.4. Melting Temperature and Latent Heat. We performed DSC on EG/CCH samples in a TA Instruments Discovery 2500 differential scanning calorimeter (DSC) using ∼5 mg samples tightly sealed in Tzero pans/Tzero hermetic lids. Samples underwent four melting/freezing cycles between 30 and 70 °C at a rate of 5 °C/min. We used Peak Integration analysis from *TRIOS* software to obtain the average melting onset temperature and enthalpies for each sample over the four cycles and calculated the average and standard deviation values. DSC data informed the selection of a TX-100 concentration and EG porosity that resulted in the expected CCH melting behavior and the highest possible latent heat storage capacity. We calculated the latter value using eq 6, which defines the enthalpy limit $\Delta H^{\circ}_{fus,max}$ based on porosity φ (calculated using eqs 2 and 3) and the enthalpy of fusion for pure CCH $\Delta H^{\circ}_{fus,CCH}$.

$$\Delta H^{\circ}_{fus,max} = \varphi \Delta H^{\circ}_{fus,CCH} \quad (6)$$

2.3.5. Supercooling and Cycling Stability. On the basis of the setup described by Marín et al.,[55] we set up a custom, calibrated temperature-history (T-history) calorimeter inside an ESPEC BTX-475 environmental chamber and used it to characterize the supercooling and cycling stability of the precompression vacuum-filtered EG-PCM composite. We placed this material in polycarbonate tubes with a high aspect ratio (ensuring 1D heat transfer), sealed the tubes with rubber plugs and epoxy, and submerged a 6-in. T-type thermocouple probe into each sample to monitor the T-history over 200 1.75-h thermal cycles between −5 and +40 °C at a frequency of 1 Hz. We calibrated the thermocouples using a constant-temperature bath and a NIST-traceable temperature probe to measure the temperature to within ±0.1 °C. On the basis of the methods described by Marín et al.[55] and Tan et al.,[56] we postprocessed the T-history data using a *MATLAB* algorithm. T-history elucidated the

https://doi.org/10.1021/acsaem.3c01223
ACS Appl. Energy Mater. 2023, 6, 8775−8786

effect of the SCH nucleating agent on the cycling stability of the EG/PCM composite.

2.3.6. Thermal Conductivity. We measured the thermal conductivity of the EG disks with and without PCM using a TA Instruments Discovery DTC-300 guarded heat flow thermal conductivity tester. Samples consisted of 50-mm-diameter and ~4-mm-thick EG disks coated with a thin layer of a Wakefield 120 series thermal joint compound, and we repeated measurements for each EG impregnation state nine times. These measurements also included mean and standard deviation values. DTC measurements allowed us to evaluate the extent of thermal conductivity enhancement provided by EG.

3. RESULTS AND DISCUSSION

3.1. EG Preparation. From left to right, Figure 3a shows the overall synthesis of the PCM composites, as described in Section 2.2. Parts b–d of Figure 3 show SEM images of EG in each stage of preparation (flake, worm, and compressed disk, respectively).

On the basis of the observed repeatability when operating the hydraulic press during EG compression, we selected three disk porosities for investigation (60%, 75%, and 90%). Additionally, we targeted a range of porosities that would reasonably constrain the experimental matrix while also providing sufficient data to determine the relationships between the porosity and composite energy density, surface modification effectiveness, and PCM impregnation rate.

Figure 3c clearly demonstrates the volumetric expansion of the graphite flakes (Figure 3b) as a result of thermal shock, where the SEM image displays the highly porous matrix present in the EG worms. Figure 3d represents a disk of 60% porosity; while the compressed matrix is clearly less porous than the worms, the SEM image demonstrates the form stability of the matrix while still retaining a porous nature.

3.2. Surface Modification. Figure 4 shows how the contact angle of a PCM drop on a compressed EG substrate changes over a span of 6 min for three EG preparation methods: unmodified, postcompression treatment, and pre-compression treatment. Figure 4 also includes examples of DSA images for each sample at the final measured increment. We prepared all EG substrates using the same compression procedure in Section 2.2 but with a much higher compression force to minimize the effect of pores on the wetting properties of EG during these experiments. A substrate with 0% porosity provides the most accurate representation of the wetting characteristics of the surface, but since achieving a true 0% porosity proved difficult with the experimental setup, the compression force and material ratios were adjusted accordingly so that the effective porosity of each sample was as low as possible and as similar as possible.

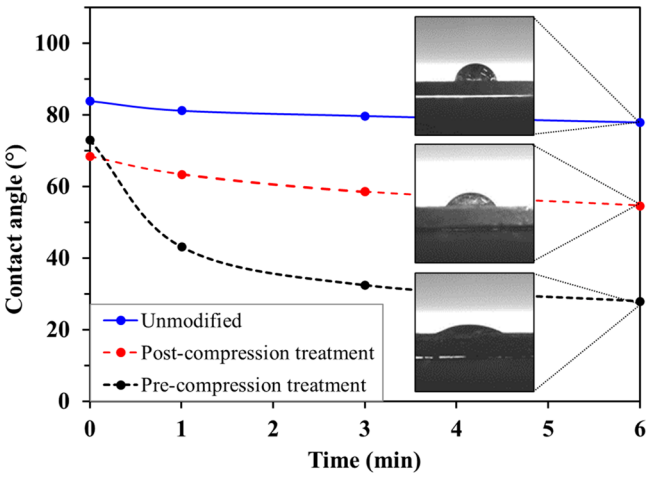

Figure 4. Contact-angle measurements for unmodified EG, EG-modified postcompression, and EG-modified precompression over 6 min, starting immediately after a PCM drop made contact with the surface of the compressed disk.

The results shown in Figure 4 suggest that regardless of the surface modification method, the presence of surfactant consistently improves the wetting of the EG substrate surface. Compared to unmodified EG, post-compression and pre-compression treatments consistently display smaller contact-angle measurements, where the magnitude of the contact angle is inversely proportional to the degree of wetting. These results indicate the successful attachment of the non-polar end of the surfactant molecule to the surface of the graphite, given the expected attraction between the polar end of the molecule to the molten salt hydrate.

EG treated with surfactant pre-compression shows the highest degree of wetting compared to unmodified EG and EG-treated post-compression. While the initial contact angle observed for the post-compression treatment sample is about 6% lower than that of the pre-compression sample, the final measurement taken after 6 min is about 95% higher. This result indicates that the pre-compression treatment is, in fact, more effective in wetting the surface of the graphite over time, suggesting faster diffusion of molten PCM into the EG pores during impregnation. For the EG disks compressed before surface modification, the results suggest that the surfactant was unable to infiltrate the inner pores of the matrix; while the outer layer of the disk was effectively modified, the inner layers were not. However, in the pre-compression treatment method, the graphite surfaces that composed the inner layers of the disk after compression were more accessible for surfactant attachment.

Figure 5 shows the DRIFTS spectra of unmodified EG and EG modified with mass fractions of TX-100 ranging from 0.01 to 0.5. For example, 0.5 TX-100:EG represents 0.5 g of TX-

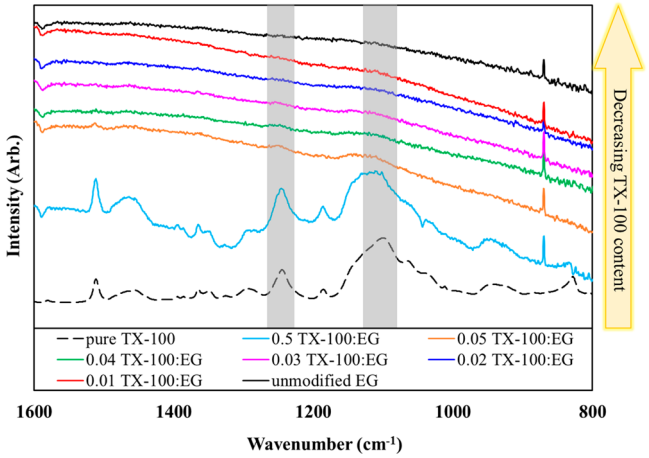

Figure 5. DRIFTS spectra for pure TX-100, pure EG, and surface-modified EG, with TX-100:EG mass ratios ranging from 0.01 to 0.5 (i.e., 0.05 TX-100:EG represents 0.05 g of TX-100 and 1 g of EG). The shaded areas correspond to the significant bands associated with TX-100.

https://doi.org/10.1021/acsaem.3c01223
ACS Appl. Energy Mater. 2023, 6, 8775–8786

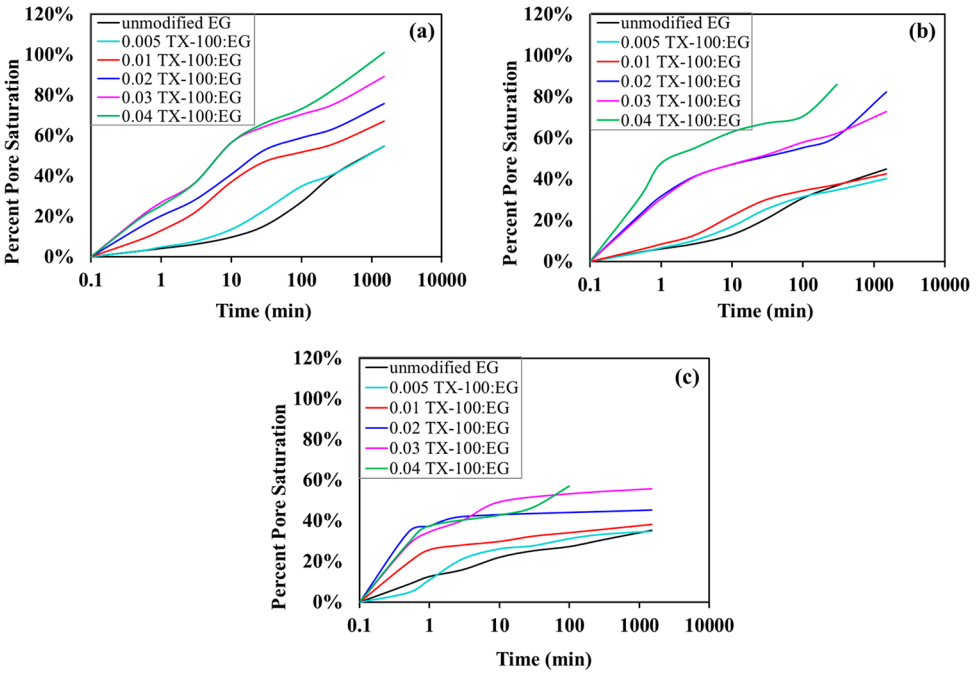

Figure 6. Percent pore saturation as a function of time with TX-100:EG mass fractions ranging from 0 to 0.05 for (a) 60%, (b) 75%, and (c) 90% EG matrix porosity. Testing and data collection were performed with 40-mm-diameter disks.

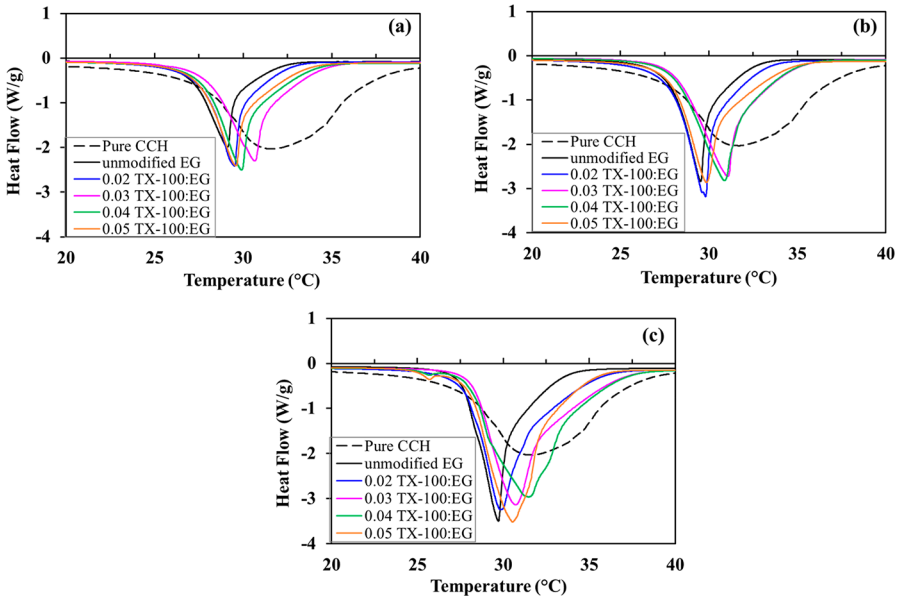

Figure 7. DSC curves for a single phase change of CCH/EG composites with TX-100:EG mass fractions ranging from 0 to 0.05 for the corresponding matrix porosities: (a) 60%, (b) 75%, and (c) 90% EG. Testing was done with 3-mm-diameter disks.

100 per 1 g of EG. To supplement the contact-angle measurements shown in Figure 4, DRIFTS spectra informed the effectiveness of EG surface modification on a molecular level, where modified EG should display the characteristic peaks associated with TX-100, indicating the successful attachment of the hydrophobic end of the molecule to the EG surface.

EG is not infrared (IR)-active (as evidenced by the spectra for unmodified EG); however, TX-100 has a number of characteristic vibrational modes. TX-100 is a nonionic surfactant with a hydrophilic poly(ethylene oxide) chain linked to hydrophobic aliphatic groups through an aromatic ring (shown in Figure 3a). At TX-100:EG mass ratios greater than or equal to 0.05, signals from symmetric and asymmetric C−O−C stretching modes indicative of the hydrophilic ethylene oxide chains (centered at 1246 and 1100 cm^{-1}, respectively[57]) are clearly present in the shaded regions shown in Figure 5. The DRIFTS signal intensity monotonically decreases with the TX-100 concentration. Although the reduced signal limits chemical structure analysis, we demonstrate successful tuning of the surfactant concentration within the composite.

3.3. Composite Energy Density. Figure 6 shows percent pore saturation of surface-modified compressed EG with PCM over the span of 1500 min for 60%, 75%, and 90% porosity, where percent pore saturation was calculated according to eqs 4 and 5, as described in Section 2.2. For these tests, we used

https://doi.org/10.1021/acsaem.3c01223
ACS Appl. Energy Mater. 2023, 6, 8775−8786

40-mm-diameter EG disks treated with surfactant pre-compression. Figure 6 also shows the effect of the TX-100 surfactant mass fraction on percent pore saturation.

In agreement with the findings shown in Figure 5, pore saturation consistently increases with the TX-100:EG mass fraction for each EG porosity, where the highest pore saturation value for each porosity occurs at a TX100:EG mass fraction of 0.04. The sample with 60% porosity reaches 100% pore saturation (Figure 6a), the sample with 75% porosity reaches around 90% saturation (Figure 6b), and the sample with 90% porosity reaches just under 60% saturation (Figure 6c).

The lower pore saturation values observed with increasing porosity are likely due to the compromised mechanical stability of the EG disks at higher porosities and higher TX-100 concentrations. Under these conditions, the disks often fell apart when removed from the PCM bath to be measured. This phenomenon also resulted in the data for the 0.04 TX-100:EG mass fraction stopping at 300 and 100 min for 75% and 90% porosity, respectively, rather than the full 1500 min like the other samples. This likely hindered the complete saturation observed in the 60% porosity sample in Figure 6a. Regardless of the soaking time and porosity, however, a 0.04 TX-100:EG mass fraction consistently resulted in the highest percent pore saturation values relative to the samples with lower TX-100 concentrations.

Figure 7 shows the results from DSC measurements taken for saturated 3-mm-diameter EG disks with the same range of TX-100 concentrations included in Figure 6.

Each sample shows good agreement (within 1 °C) between the phase change onset temperature of the composite and that of pure CCH, where the difference between the two values converges as the porosity of the EG matrix increases. The enthalpy of the samples was calculated based on the integral (area under the curve) of each curve, where the width of the dip is dependent on the ramp rate and conductivity of the material. This value is also representative of temperature glide, an intrinsic PCM property that corresponds to the speed of heat transfer. Compared to curves for pure CCH, the impregnated EG samples show a steeper slope (higher magnitude of heat flow over a smaller temperature range), indicating that the rate of heat transfer is improved in the presence of EG. This finding corroborates the addition of EG for thermal conductivity enhancement.

Table 2 includes enthalpy values corresponding to each curve in Figure 7, calculated using *TRIOS* peak integration software. The area under the curve is equivalent to the enthalpy in joules per gram. The values in Table 2 also correspond to the points in Figure 8.

Figure 8 shows the values for the phase change onset temperature and enthalpy corresponding to each curve in Figure 6, where pure CCH has a phase change onset temperature of 28 °C (standard deviation of 0.5 °C) and an enthalpy of 197 J/g (standard deviation of 12 J/g). The red dashed line represents the phase change onset temperature of pure CCH, and the blue dashed line represents the theoretical maximum enthalpy that could be achieved for each porosity, calculated using eq 6, as described in Section 2.3. The red- and blue-shaded regions represent the standard deviations for each respective parameter.

Nearly all composite samples show a phase change onset temperature within the standard deviation for that of pure CCH, suggesting that the presence of EG and TX-100 has little-to-no effect on the melting behavior of the PCM in the composite. However, Figure 8 shows that porosity does appear to be correlated with phase change onset: as the porosity increases, the average distance between the experimental data points and the pure CCH onset temperature decreases. The depressed melting temperatures at lower porosities are likely a result of increased confinement effects for solid−liquid transitions at smaller pore sizes,[58] a phenomenon that has been corroborated for salt hydrates in porous media.[59] While the pore size was not a parameter measured in this work, studies have shown a relationship between the pore size and porosity, where lower porosity corresponds to smaller pore size.[60]

Table 2. Enthalpy Values Collected via DSC for Pure CCH and CCH/EG Composites with TX-100:EG Mass Ratios Ranging from 0 to 0.05 (i.e., 0.02 TX-100:EG Represents an EG Matrix Surface-Modified Using 0.02 g of TX-100 per 1 g of EG)[a]

	Enthalpy (J/g)		
	60% porosity	75% porosity	90% porosity
Pure CCH	197 ± 12	197 ± 12	197 ± 12
Unmodified EG	71.3 ± 0.2	93.7 ± 1.8	129 ± 7.0
0.02 TX-100:EG	87 ± 3.0	120 ± 0.4	170 ± 2.0
0.03 TX-100:EG	103.5 ± 1.4	123.3 ± 1.2	174.2 ± 0.2
0.04 TX-100:EG	105.5 ± 0.6	130 ± 3.0	183 ± 0.3
0.05 TX-100:EG	97.9 ± 0.1	126.6 ± 0.6	177.2 ± 0.5

[a]Enthalpy values correspond to the curves in Figure 7 and points in Figure 8. Standard deviation corresponds to the value following the ± sign.

The convergence of the experimental data for EG/CCH composites and the values for pure CCH are also observed to some extent in the enthalpy measurements. Parts a and b of Figure 8 (60% and 75% porosity, respectively) both show that all measured enthalpy values are outside of the blue-shaded region, representing the maximum possible enthalpy for that given porosity, whereas Figure 8c (90% porosity) shows four measured values within the shaded region. This suggests that higher porosities do, in fact, allow a greater extent of pore saturation, and thus higher relative volumes of PCM, to be contained in the composite. In comparison to Figure 6, which suggests a decreasing degree of pore saturation with increasing porosity, the samples used for Figures 7 and 8 were not constrained by mechanical instability during testing due to the small sample size.

The highest enthalpy for each porosity is observed when the TX-100:EG mass fraction is 0.04, strongly indicating that this concentration offers the best thermal performance regardless of the porosity, which is consistent with the results shown in Figure 6. The drop in enthalpy observed in the TX-100:EG mass fraction of 0.05 indicates that there is a threshold where effective surface modification transitions into pore clogging. According to the results shown in Figure 8, a TX-100:EG mass fraction above 0.04 may lead to excess surfactant present in EG pores, effectively inhibiting the infiltration of PCM rather than enabling it.

3.4. Supercooling and Cycling Stability. While the DSC results shown in Figure 7 are valuable, long-term thermal cycling behavior can be analyzed more effectively using the T-history method. T-history can more accurately identify the prevalence of PCM challenges such as supercooling and phase separation because of the larger amounts of sample used for

https://doi.org/10.1021/acsaem.3c01223
ACS Appl. Energy Mater. 2023, 6, 8775−8786

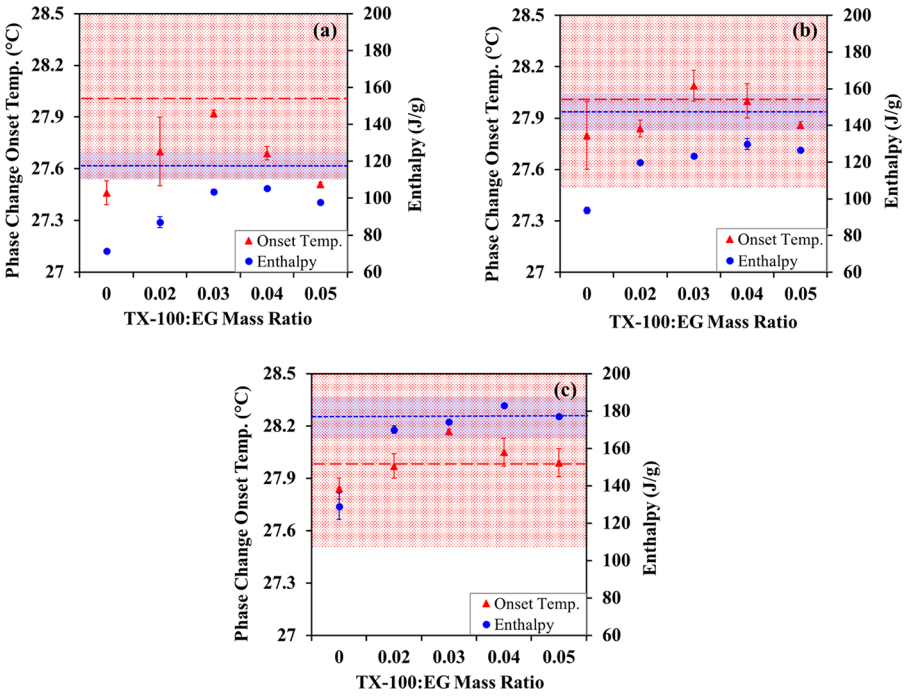

Figure 8. Phase change onset temperature and enthalpy of CCH/EG composites as a function of the TX-100:EG mass ratio for EG matrixes of (a) 60%, (b) 75%, and (c) 90% porosity. Values were extracted from the DSC data shown in Figure 6 and summarized in Table 2. The red dashed lines represent the average values for the onset temperature of pure CCH and the blue dashed lines represent the maximum possible composite enthalpy for each porosity (with the standard deviation for each shown in the shaded regions with corresponding colors).

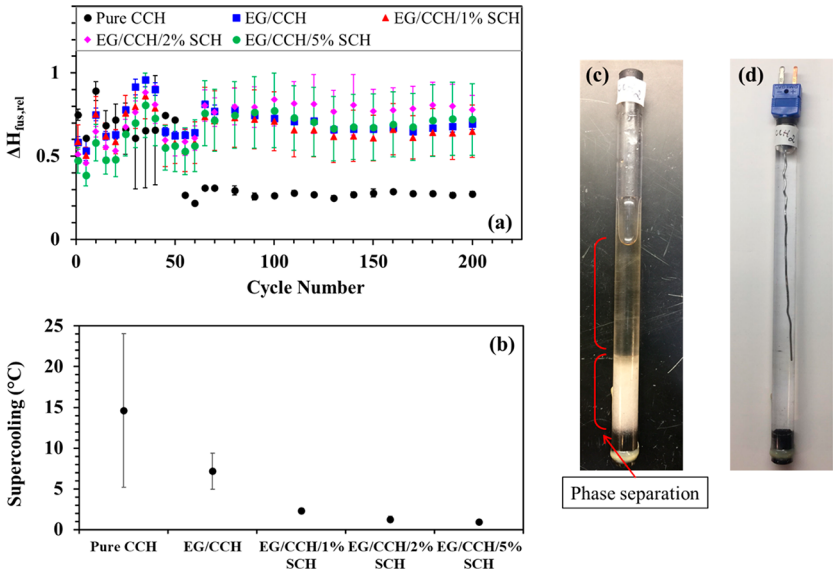

Figure 9. (a) Relative latent heat of fusion over 200 thermal cycles with respect to maximum values for pure CCH, EG impregnated with CCH, and EG impregnated with CCH and 1, 2, and 5 wt % SCH. (b) Average degree of supercooling over 50 thermal cycles for pure CCH and 200 cycles for EG impregnated with CCH and EG impregnated with CCH and 1, 2, and 5 wt % SCH. (c) Example of visible pure CCH phase separation. (d) Example of a T-history test-tube setup with a thermocouple (minimal sample included to better display the setup).

testing, and thus this method can more reliably evaluate the effectiveness of the EG matrix and SCH nucleating agent in providing heterogeneous nucleation sites. T-history experiments involve test tubes filled with composite material (Figure 9d) and placed in a temperature-controlled environmental chamber, as described in Section 2.3.

The results shown in Figure 9a represent the cycling stability: the plot displays the relative latent heat storage capacity for pure CCH, EG impregnated with CCH and no nucleating agent, and EG impregnated with CCH and 1, 2, and 5 wt % SCH, where the reference value is the maximum recorded enthalpy for each respective sample. The enthalpy of all samples fluctuates throughout the first 70 cycles, after which the latent heat of fusion of the EG/CCH composite samples stabilizes and remains nearly constant for the rest of the experiment, suggesting no phase separation. However, the pure CCH sample shows a precipitous drop in enthalpy after 50 cycles, after which the enthalpy does not recover. The drop in

https://doi.org/10.1021/acsaem.3c01223
ACS Appl. Energy Mater. 2023, 6, 8775−8786

the latent heat observed for pure CCH indicates phase separation, an example of which is shown in Figure 9c. Between the EG/CCH composite samples, there is no clear trend regarding the presence and amount of SCH nucleating agent. Figure 9a does not suggest that SCH has a detrimental effect on the cycling stability and phase separation, but the results also do not suggest that SCH plays a significant role in retaining enthalpy. Rather, EG is the primary component responsible for mitigation of phase separation, as indicated by the clear difference in the enthalpy stability between pure CCH and all other samples.

Figure 9b shows the average degree of supercooling for the same set of samples shown in Figure 9a, calculated by the difference between the phase transition temperature and the temperature at which the sample nucleated, where lower supercooling values indicate a more successful nucleation of the sample. The pure CCH sample shown includes only supercooling values up to cycle 50 because the phase change and nucleation temperatures recorded for the subsequent cycles were distorted due to phase separation (as shown in Figure 9a). The average supercooling values for the remaining samples containing EG include data from all 200 cycles, however. Figure 9b further distinguishes the respective roles of EG and SCH in the composite: while Figure 9a only definitively shows that EG, not SCH, aids in decreasing the phase separation and increasing the cycling stability, Figure 9b shows a synergistic effect between the two materials in combating supercooling. When EG is introduced, the degree of supercooling decreases by 51% compared to that of pure CCH. When 1, 2, and 5 wt % SCH is added, the degree of supercooling decreases by an additional 68%, 83%, and 87% compared to those of EG/CCH, respectively.

The EG/CCH composite with 5 wt % SCH shows the smallest degree of supercooling at 0.95 °C. While samples without EG (i.e., only CCH + SCH) were not tested, studies examining a similar range of SCH concentrations for CCH nucleation also found decreasing degrees of supercooling with increasing SCH concentrations, reaching a minimum of 2.8−2.51 °C.[48,51] On the basis of phase separation and supercooling, the results of our T-history experiments display a high degree of cycling stability over 200 cycles, which stands out in the literature. Based on the results shown in parts a and b of Figure 9, a concentration of 5 wt % SCH in an EG/CCH composite can be considered the composition most likely to provide a stable, reliable thermal performance.

3.5. Thermal Conductivity. Figure 10 shows the thermal conductivity over a temperature range of 15−80 °C for unmodified compressed EG and modified compressed EG, as well as the thermal conductivity of modified compressed EG impregnated with CCH over a temperature range of 15−20 °C to avoid a phase change during measurements. Each set of data includes EG matrixes of 60%, 75%, and 90% porosity, and the modified EG contains a TX-100:EG mass fraction of 0.04 based on the results from pore saturation and DSC testing (Figures 6 and 7, respectively). The error bars represent the standard deviation of the thermal conductivity values for each sample over the temperature range measured, effectively displaying the dependence of the thermal conductivity on temperature.

The thermal conductivity of unmodified, compressed EG demonstrates a slight dependence on porosity: thermal conductivity increases with porosity due to better percolation of the EG matrix at lower compression forces (i.e., higher porosity). As the compression force increases and the porosity decreases, the 2D graphene layers in EG transform from a hexagonal configuration to a sheetlike configuration, causing more phonon scattering at the sheet interfaces and a decrease in the thermal conductivity when it is measured perpendicular to the plane of the graphene sheets.[64] When EG is modified, this phenomenon is even more clear: while the 90% porosity sample has a thermal conductivity similar to that of unmodified EG, the 60% and 75% samples show a discernible decrease from their unmodified EG counterparts. In the case of surface-modified EG, the presence of surfactant on the sheet surface compounds effects the phonon scattering by adding another interface, further decreasing the thermal conductivity.[65]

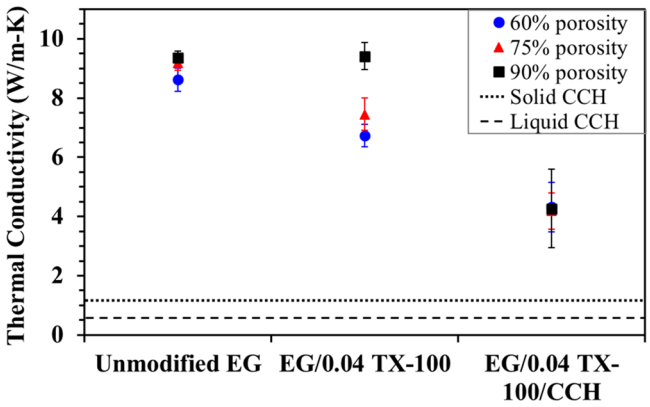

Figure 10. Thermal conductivity between 15 and 80 °C for unmodified EG disks and surface-modified EG disks, and thermal conductivity between 15 and 20 °C for surface-modified EG disks impregnated with CCH. Each sample was tested with EG disk porosities of 60, 75, and 90%. All samples with modified EG used a TX-100-EG mass fraction of 0.04. Dashed lines represent the thermal conductivity values for pure solid and liquid CCH, respectively, as reported in the literature.[61−63]

However, when the modified EG matrix is impregnated with CCH, the dependence on the porosity is much less significant. Compared to the samples without CCH, the impregnated sample shows a significant decrease in the thermal conductivity irrespective of the porosity, corroborating the importance of thermal conductivity when considering challenges to the PCM performance and further illustrating the effects of phonon scattering. The thermal conductivity of the impregnated sample displays a greater dependence on the temperature, as indicated by the larger standard deviation error bars, where the thermal conductivity increases with temperature.

Despite the fact that the impregnated samples have notably lower thermal conductivity values than those of unmodified and modified EG, shifting the frame of reference from EG to pure CCH demonstrates the effectiveness of EG in increasing the thermal conductivity of the composite. Several studies report the thermal conductivity of pure CCH as ∼1.09 W/mK in the solid state and ∼0.55 W/mK in the liquid state, as shown by the dashed lines,[61−63] so although the impregnated sample has a thermal conductivity about 60% lower than that of unmodified EG, its thermal conductivity is about 290% greater than that of solid CCH.

4. CONCLUSIONS

This study describes the development of a novel, form-stable PCM composite that has the potential to increase buildings' thermal performance and thermal comfort through integration

https://doi.org/10.1021/acsaem.3c01223
ACS Appl. Energy Mater. 2023, 6, 8775−8786

into systems such as HVAC. The composite consists of an inorganic salt hydrate PCM ($CaCl_2{\cdot}6H_2O$) paired with a lattice-matched nucleating agent ($SrCl_2{\cdot}6H_2O$), impregnated into a porous matrix of EG modified for hydrophilicity using nonionic surfactant TX-100.

The results of this study demonstrate successful the surface modification of EG at a TX-100:EG mass fraction of 0.04, leading to a high degree of pore saturation for a range of EG matrix porosities. In combination with the added surface area provided by EG, a 5% SCH concentration resulted in a composite with only 0.95 °C of supercooling. The composite achieved a latent heat of 183 J/g, only 7% lower than that of pure CCH and well within the standard deviation of the theoretical maximum enthalpy for that porosity. Over 200 thermal cycles, T-history testing showed a minimal reduction in the level of latent heat along with no phase separation. The incorporation of EG into the composite also resulted in a thermal conductivity 290% greater than that of pure CCH.

These findings stand out among existing literature on inorganic PCM composites because of the combination of minimal supercooling, high relative energy storage density, successful enhancement of thermal conductivity, and excellent cycling stability over 200 cycles using sample sizes more representative of practical applications (compared to DSC). The use of relatively low-cost and accessible materials along with simple fabrication steps opens doors for the use of this technology in a wide range of building applications from incorporation into HVAC systems, heat exchanger systems, or building envelope design.

■ ASSOCIATED CONTENT

Data Availability Statement

The raw data required to reproduce these findings are available upon request.

■ AUTHOR INFORMATION

Corresponding Author

Adewale Odukomaiya − *National Renewable Energy Laboratory, Golden, Colorado 80401, United States;* orcid.org/0000-0002-9560-9964; Email: Adewale.Odukomaiya@nrel.gov

Authors

Erin Blackley − *National Renewable Energy Laboratory, Golden, Colorado 80401, United States; Colorado School of Mines, Golden, Colorado 80401, United States;* orcid.org/0000-0002-9483-924X

Trinny Lai − *National Renewable Energy Laboratory, Golden, Colorado 80401, United States*

Paulo Cesar Tabares-Velasco − *Colorado School of Mines, Golden, Colorado 80401, United States;* orcid.org/0000-0001-5401-7594

Lance M. Wheeler − *National Renewable Energy Laboratory, Golden, Colorado 80401, United States;* orcid.org/0000-0002-1685-8242

Jason Woods − *National Renewable Energy Laboratory, Golden, Colorado 80401, United States;* orcid.org/0000-0002-7661-2658

Complete contact information is available at: https://pubs.acs.org/10.1021/acsaem.3c01223

Notes

The authors declare no competing financial interest.

■ ACKNOWLEDGMENTS

This work was authored in part by the National Renewable Energy Laboratory (NREL), operated by Alliance for Sustainable Energy, LLC, for the U.S. Department of Energy (DOE) under Contract DE-AC36-08GO28308. This work was supported by the Laboratory Directed Research and Development Program at NREL. The views expressed in the article do not necessarily represent the views of the DOE or the U.S. Government. The U.S. Government retains and the publisher, by accepting the article for publication, acknowledges that the U.S. Government retains a nonexclusive, paid-up, irrevocable, worldwide license to publish or reproduce the published form of this work, or allow others to do so, for U.S. Government purposes. The authors acknowledge Judith Vidal and Roderick Jackson for providing scientific direction and input.

■ REFERENCES

(1) Al-Yasiri, Q.; Szabó, M. Incorporation of Phase Change Materials into Building Envelope for Thermal Comfort and Energy Saving: A Comprehensive Analysis. *J. Build. Eng.* **2021**, *36*, 102122.

(2) Gonzalez-Torres, M.; Perez-Lombard, L.; Coronel, J. F.; Maestre, I. R.; Yan, D. A Review on Buildings Energy Information: Trends, End-Uses, Fuels and Drivers. *Energy Rep* **2022**, *8*, 626−637.

(3) Chai, J.; Fan, J. Advanced Thermal Regulating Materials and Systems for Energy Saving and Thermal Comfort in Buildings. *Mater. Today Energy* **2022**, *24*, 100925.

(4) Sherman, P.; Lin, H.; McElroy, M. Projected Global Demand for Air Conditioning Associated with Extreme Heat and Implications for Electricity Grids in Poorer Countries. *Energy Build* **2022**, *268*, 112198.

(5) Heier, J.; Bales, C.; Martin, V. Combining Thermal Energy Storage with Buildings − a Review. *Renew. Sustain. Energy Rev.* **2015**, *42*, 1305−1325.

(6) Rathore, P. K. S.; Gupta, N. K.; Yadav, D.; Shukla, S. K.; Kaul, S. Thermal Performance of the Building Envelope Integrated with Phase Change Material for Thermal Energy Storage: An Updated Review. *Sustain. Cities Soc.* **2022**, *79*, 103690.

(7) Hu, Y.; Heiselberg, P. K.; Drivsholm, C.; Søvsø, A. S.; Vogler-Finck, P. J. C.; Kronby, K. Experimental and Numerical Study of PCM Storage Integrated with HVAC System for Energy Flexibility. *Energy Build* **2022**, *255*, 111651.

(8) Said, M. A.; Hassan, H. An Experimental Work on the Effect of Using New Technique of Thermal Energy Storage of Phase Change Material on the Performance of Air Conditioning Unit. *Energy Build* **2018**, *173*, 353−364.

(9) Hong, T.; Wang, S.; Wang, F.; Wang, X. Experimental Study on the Demand Shifting Effects of PCM Integrated Air-Conditioning Duct. *IOP Conf. Ser. Earth Environ. Sci.* **2019**, *238* (1), 012048.

(10) Pielichowska, K.; Pielichowski, K. Phase Change Materials for Thermal Energy Storage. *Prog. Mater. Sci.* **2014**, *65*, 67−123.

(11) Yang, T.; King, W. P.; Miljkovic, N. Phase Change Material-Based Thermal Energy Storage. *Cell Rep. Phys. Sci.* **2021**, *2* (8), 100540.

(12) Zhou, D.; Zhao, C. Y.; Tian, Y. Review on Thermal Energy Storage with Phase Change Materials (PCMs) in Building Applications. *Appl. Energy* **2012**, *92*, 593−605.

(13) Li, Y.; Li, C.; Lin, N.; Xie, B.; Zhang, D.; Chen, J. Review on Tailored Phase Change Behavior of Hydrated Salt as Phase Change Materials for Energy Storage. *Mater. Today Energy* **2021**, *22*, 100866.

(14) Hirschey, J.; Gluesenkamp, K. R.; Mallow, A.; Graham, S. Review of Inorganic Salt Hydrates with Phase Change Temperature in Range of 5°C to 60°C and Material Cost Comparison with Common Waxes. *5th International High Performance Buildings Conference at Purdue*, West Lafayette, IN, July 9−12, 2018; Purdue University, 2018; p 3653.

(15) Dixit, P.; Reddy, V. J.; Parvate, S.; Balwani, A.; Singh, J.; Maiti, T. K.; Dasari, A.; Chattopadhyay, S. Salt Hydrate Phase Change

Materials: Current State of Art and the Road Ahead. *J. Energy Storage* **2022**, *51*, 104360.
(16) Beaupere, N.; Soupremanien, U.; Zalewski, L. Nucleation Triggering Methods in Supercooled Phase Change Materials (PCM), a Review. *Thermochim. Acta* **2018**, *670*, 184−201.
(17) Belton, G.; Ajami, F. *Thermochemistry of Salt Hydrates; PB-227966*; National Center for Energy Management and Power: Philadelphia, PA, 1973.
(18) Günther, E. Sononucleation of Inorganic Phase Change Materials. Ph.D. Dissertation, Technical University of Munich, Munich, Germany, 2011.
(19) Cui, W.; Zhang, H.; Xia, Y.; Zou, Y.; Xiang, C.; Qiu, S.; Xu, F.; Sun, L.; Chu, H. Preparation and Thermophysical Properties of a Novel Form-Stable $CaCl_2{\cdot}6H_2O$/Sepiolite Composite Phase Change Material for Latent Heat Storage. *J. Therm. Anal. Calorim.* **2018**, *131*, 57−63.
(20) Liu, S.; Yang, H. Porous Ceramic Stabilized Phase Change Materials for Thermal Energy Storage. *RSC Adv.* **2016**, *6* (53), 48033−48042.
(21) Purohit, B. K.; Sistla, V. S. Studies on Solution Crystallization of Na2SO4·10H2O Embedded in Porous Polyurethane Foam for Thermal Energy Storage Application. *Thermochim. Acta* **2018**, *668*, 9−18.
(22) Wu, Y.; Wang, T. Preparation and Characterization of Hydrated Salts/Silica Composite as Shape-Stabilized Phase Change Material via Sol−Gel Process. *Thermochim. Acta* **2014**, *591*, 10−15.
(23) Lane, G. A. Phase Change Materials for Energy Storage Nucleation to Prevent Supercooling. *Sol. Energy Mater. Sol. Cells* **1992**, *27* (2), 135−160.
(24) Ryu, H. W.; Woo, S. W.; Shin, B. C.; Kim, S. D. Prevention of Supercooling and Stabilization of Inorganic Salt Hydrates as Latent Heat Storage Materials. *Sol. Energy Mater. Sol. Cells* **1992**, *27* (2), 161−172.
(25) Shin, B. C.; Kim, S. D.; Won-Hoon, P. Phase Separation and Supercooling of a Latent Heat-Storage Material. *Energy* **1989**, *14* (12), 921−930.
(26) Fan, L.; Khodadadi, J. M. Thermal Conductivity Enhancement of Phase Change Materials for Thermal Energy Storage: A Review. *Renew. Sustain. Energy Rev.* **2011**, *15* (1), 24−46.
(27) Zhang, P.; Xiao, X.; Ma, Z. W. A Review of the Composite Phase Change Materials: Fabrication, Characterization, Mathematical Modeling and Application to Performance Enhancement. *Appl. Energy* **2016**, *165*, 472−510.
(28) Wu, S.; Yan, T.; Kuai, Z.; Pan, W. Thermal Conductivity Enhancement on Phase Change Materials for Thermal Energy Storage: A Review. *Energy Storage Mater.* **2020**, *25*, 251−295.
(29) Barthwal, M.; Dhar, A.; Powar, S. Effect of Nanomaterial Inclusion in Phase Change Materials for Improving the Thermal Performance of Heat Storage: A Review. *ACS Appl. Energy Mater.* **2021**, *4* (8), 7462−7480.
(30) Zhou, W.; Jiang, J.; Wu, H.; Hu, D.; Li, P.; Yang, X.; Jia, X. Facile Preparation of Binary Salt Hydrates/Carbon Nanotube Composite for Thermal Storage Materials with Enhanced Structural Stability. *ACS Appl. Energy Mater.* **2021**, *4* (5), 4561−4569.
(31) Wu, Y.; Wang, T. Hydrated Salts/Expanded Graphite Composite with High Thermal Conductivity as a Shape-Stabilized Phase Change Material for Thermal Energy Storage. *Energy Convers. Manag.* **2015**, *101*, 164−171.
(32) Zhou, Y.; Sun, W.; Ling, Z.; Fang, X.; Zhang, Z. Hydrophilic Modification of Expanded Graphite to Prepare a High-Performance Composite Phase Change Block Containing a Hydrate Salt. *Ind. Eng. Chem. Res.* **2017**, *56* (50), 14799−14806.
(33) Zhou, S.; Zhou, Y.; Ling, Z.; Zhang, Z.; Fang, X. Modification of Expanded Graphite and Its Adsorption for Hydrated Salt to Prepare Composite PCMs. *Appl. Therm. Eng.* **2018**, *133*, 446−451.
(34) Zhang, Y.; Sun, J.; Ma, G.; Wang, Z.; Xie, S.; Jing, Y.; Jia, Y. Hydrophilic Expanded Graphite-Magnesium Nitrate Hexahydrate Composite Phase Change Materials: Understanding the Effect of Hydrophilic Modification on Thermophysical Properties. *Int. J. Energy Res.* **2019**, *43* (3), 1121−1132.
(35) Chung, D. D. L. A. Review of Exfoliated Graphite. *J. Mater. Sci.* **2016**, *51* (1), 554−568.
(36) Bonnissel, M.; Luo, L.; Tondeur, D. Compacted Exfoliated Natural Graphite as Heat Conduction Medium. *Carbon* **2001**, *39* (14), 2151−2161.
(37) Kim, S.; Drzal, L. T. High Latent Heat Storage and High Thermal Conductive Phase Change Materials Using Exfoliated Graphite Nanoplatelets. *Sol. Energy Mater. Sol. Cells* **2009**, *93* (1), 136−142.
(38) Mills, A.; Farid, M.; Selman, J. R.; Al-Hallaj, S. Thermal Conductivity Enhancement of Phase Change Materials Using a Graphite Matrix. *Appl. Therm. Eng.* **2006**, *26* (14−15), 1652−1661.
(39) Py, X.; Olives, R.; Mauran, S. Paraffin/Porous-Graphite-Matrix Composite as a High and Constant Power Thermal Storage Material. *Int. J. Heat Mass Transfer* **2001**, *44* (14), 2727−2737.
(40) Zhao, J.; Guo, Y.; Feng, F.; Tong, Q.; Qy, W.; Wang, H. Microstructure and Thermal Properties of a Paraffin/Expanded Graphite Phase-Change Composite for Thermal Storage. *Renew. Energy* **2011**, *36* (5), 1339−1342.
(41) Zhong, Y.; Li, S.; Wei, X.; Liu, Z.; Guo, Q.; Shi, J.; Liu, L. Heat Transfer Enhancement of Paraffin Wax Using Compressed Expanded Natural Graphite for Thermal Energy Storage. *Carbon* **2010**, *48* (1), 300−304.
(42) Mallow, A.; Abdelaziz, O.; Graham, S. Thermal Charging Performance of Enhanced Phase Change Material Composites for Thermal Battery Design. *Int. J. Therm. Sci.* **2018**, *127*, 19−28.
(43) Mallow, A.; Abdelaziz, O.; Graham, S. Thermal Charging Study of Compressed Expanded Natural Graphite/Phase Change Material Composites. *Carbon* **2016**, *109*, 495−504.
(44) Mallow, A.; Abdelaziz, O.; Kalaitzidou, K.; Graham, S. Investigation of the Stability of Paraffin−Exfoliated Graphite Nanoplatelet Composites for Latent Heat Thermal Storage Systems. *J. Mater. Chem.* **2012**, *22* (46), 24469.
(45) Xiao, C.; Wu, X.; Dong, X.; Ye, G.; Zhang, G.; Yang, X. Ultrareliable Composite Phase Change Material for Battery Thermal Management Derived from a Rationally Designed Phase Changeable and Hydrophobic Polymer Skeleton. *ACS Appl. Energy Mater.* **2021**, *4* (4), 3832−3841.
(46) Li, F.; Zhen, H.; Li, L.; Li, Y.; Wang, Q.; Cheng, X. A Template-Method Synthesis of Mesoporous-MgO/Expanded Graphite for Enhancing Thermal Properties of Methyl Palmitate-Lauric Acid Phase Change Materials. *Mater. Today Energy* **2022**, *26*, 100999.
(47) Duan, Z.; Zhang, H.; Sun, L.; Cao, Z.; Xu, F.; Zou, Y.; Chu, H.; Qiu, S.; Xiang, C.; Zhou, H. $CaCl_2{\cdot}6H_2O$/Expanded Graphite Composite as Form-Stable Phase Change Materials for Thermal Energy Storage. *J. Therm. Anal. Calorim.* **2014**, *115* (1), 111−117.
(48) Li, X.; Zhou, Y.; Nian, H.; Ren, X.; Dong, O.; Hai, C.; Shen, Y.; Zeng, J. Phase Change Behavior of Latent Heat Storage Media Based on Calcium Chloride Hexahydrate Composites Containing Strontium Chloride Hexahydrate and Oxidation Expandable Graphite. *Appl. Therm. Eng.* **2016**, *102*, 38−44.
(49) Xin, Y.; Nian, H.; Li, J.; Zhao, J.; Tan, X.; Zhou, Y.; Zhu, F.; Liu, H.; Li, X. Effect of $NiCo_2O_4$-Modified Expanded Graphite on Heat Transfer and Storage Improvement of $CaCl_2{\cdot}6H_2O$. *J. Energy Storage* **2022**, *46*, 103902.
(50) Jin, Z.; Tian, Y.; Xu, X.; Cui, H.; Tang, W.; Yun, Y.; Sun, G. Experimental Investigation on Graphene Oxide/$SrCl_2{\cdot}6H_2O$ Modified $CaCl_2{\cdot}6H_2O$ and the Resulting Thermal Performances. *Materials* **2018**, *11* (9), 1507.
(51) Niu, D.; Tan, Y.; Zhang, T.; Zhang, X.; Zhang, W. Thermal Properties and Application of a Novel $CaCl_2{\cdot}6H_2O$/Expanded Graphite Shape-Stabilized Composite Phase Change Material for Electric Radiant Heating. *J. Energy Storage* **2022**, *55*, 105458.
(52) Mehling, H.; Cabeza, L. F. *Heat and Cold Storage with PCM: An Up to Date Introduction into Basics and Applications*; Mewes, D., Mayinger, F., Series, Eds.; Heat and Mass Transfer Series; Springer: Berlin, 2008. DOI: 10.1007/978-3-540-68557-9.

(53) Odukomaiya, A.; Blackley, E.; Woods, J.; Vidal, J.; Cui, S. Salt Hydrate-Based Phase Change Thermal Energy Storage and Encapsulation Thereof. U.S. Patent US 11560504 B2, 2023.
(54) Roberts, W. L.; Rapp, G. R.; Cambell, T. J. *Encyclopedia of Minerals*; Springer USA, 1990.
(55) Marín, J. M.; Zalba, B.; Cabeza, L. F.; Mehling, H. Determination of Enthalpy Temperature Curves of Phase Change Materials with the Temperature-History Method: Improvement to Temperature Dependent Properties. *Meas. Sci. Technol.* **2003**, *14* (2), 184−189.
(56) Tan, P.; Brütting, M.; Vidi, S.; Ebert, H.-P.; Johansson, P.; Sasic Kalagasidis, A. Characterizing Phase Change Materials Using the T-History Method: On the Factors Influencing the Accuracy and Precision of the Enthalpy-Temperature Curve. *Thermochim. Acta* **2018**, *666*, 212−228.
(57) Coates, J. Interpretation of Infrared Spectra, A Practical Approach. *Encyclopedia of Analytical Chemistry*; John Wiley & Sons, Ltd., 2006. DOI: 10.1002/9780470027318.a5606.
(58) Sliwinska-Bartkowiak, M.; Gras, J.; Sikorski, R.; Radhakrishnan, R.; Gelb, L.; Gubbins, K. E. Phase Transitions in Pores: Experimental and Simulation Studies of Melting and Freezing. *Langmuir* **1999**, *15* (18), 6060−6069.
(59) Wu, Y.; Wang, T. The Dependence of Phase Change Enthalpy on the Pore Structure and Interfacial Groups in Hydrated Salts/Silica Composites via Sol−Gel. *J. Colloid Interface Sci.* **2015**, *448*, 100−105.
(60) Mauran, S.; Rigaud, L.; Coudevylle, O. Application of the Carman−Kozeny Correlation to a High-Porosity and Anisotropic Consolidated Medium: The Compressed Expanded Natural Graphite. *Transp. Porous Media* **2001**, *43* (2), 355−376.
(61) Dinçer, İ.; Rosen, M. A. *Thermal Energy Storage: Systems and Applications*, 1st ed.; John Wiley & Sons, Ltd., 2002.
(62) Lane, G. A. Low Temperature Heat Storage with Phase Change Materials. *Int. J. Ambient Energy* **1980**, *1* (3), 155−168.
(63) Tyagi, V. V.; Buddhi, D. Thermal Cycle Testing of Calcium Chloride Hexahydrate as a Possible PCM for Latent Heat Storage. *Sol. Energy Mater. Sol. Cells* **2008**, *92* (8), 891−899.
(64) Sadeghi, M. M.; Jo, I.; Shi, L. Phonon-Interface Scattering in Multilayer Graphene on an Amorphous Support. *Proc. Natl. Acad. Sci. U. S. A.* **2013**, *110* (41), 16321−16326.
(65) Chen, G. Phonon Heat Conduction in Nanostructures. *Int. J. Therm. Sci.* **2000**, *39* (4), 471−480.